Structural models of $FeSe_x$

2009 J. Phys.: Condens. Matter 21 435702

(http://iopscience.iop.org/0953-8984/21/43/435702)

J. Phys.: Condens. Matter **21** (2009) 435702 (6pp) doi:10.1088/0953-8984/21/43/435702

Structural models of $FeSe_x$

E Z Kurmaev[1], J A McLeod[2], N A Skorikov[1], L D Finkelstein[1], A Moewes[2], M A Korotin[1], Yu A Izyumov[1], Y L Xie[3], G Wu[3] and X H Chen[3]

[1] Institute of Metal Physics, Russian Academy of Sciences—Ural Division, 620219 Yekaterinburg, Russia
[2] Department of Physics and Engineering Physics, University of Saskatchewan, 116 Science Place, Saskatoon, Saskatchewan S7N 5E2, Canada
[3] Hefei National Laboratory for Physical Science at the Microscale and Department of Physics, University of Science and Technology of China, Hefei, Anhui 230026, People's Republic of China

E-mail: john.mcleod@usask.ca

Received 17 July 2009, in final form 28 August 2009
Published 9 October 2009
Online at stacks.iop.org/JPhysCM/21/435702

Abstract
Two different structural models for non-stoichiometric $FeSe_x$ are examined and compared with soft x-ray spectroscopy findings for $FeSe_x$ ($x = 0.85, 0.50$). A structural model of tetragonal FeSe with excess interstitial Fe gives better agreement with experiment than a structural model of tetragonal FeSe with Se vacancies. This interstitial Fe increases the number of 3d states at the Fermi level. We find evidence that large non-stoichiometric ratios of Fe:Se, such as that of $FeSe_{0.50}$, yield clusters of pure Fe in the crystal structure.

1. Introduction

Recently, the family of Fe-based superconductors, consisting mainly of FeAs compounds [1–3], has expanded to include $Fe(Se/Te)_x$-compounds [4]. A T_c of approximately 8 K has been reported for $FeSe_x$ at ambient pressure [4], and an increase in T_c to 27 K with the application of 1.48 GPa has been reported for FeSe [5].

FeSe has a PbO-type crystal structure composed of planar layers of Fe_2Se_2. These layers are analogous to the Fe_2As_2 layers common to the FeAs family of superconductors. In the FeAs family of superconductors, however, there is an additional planar layer, either ReO layers in the ReOFeAs series, Ae layers in the $AeFe_2As_2$ series, or Li(Na) layers in the Li(Na)FeAs compounds (where Re and Ae are rare-earths and alkaline earths, respectively). Because FeSe has only one type of planar layer, this material is preferable over FeAs compounds in the study of magnetic order, electronic structure, and physical properties. Band structure calculations of Subedi *et al* [6] reveal that FeSe has cylindrical Fermi surfaces, both for electrons and holes, similar to the Fermi surface of FeAs compounds. These Fermi surfaces satisfy the nesting conditions that result in spin density wave (SDW) instability and the appearance of an antiferromagnetic ground state. These experimental findings have been confirmed by angle-resolved photo-emission spectroscopy (ARPES) measurements [7]. Both experiments and calculations suggest there is an interplay between superconductivity and magnetism in tetragonal FeSe, analogous to the situation for the FeAs superconducting compounds.

It has been found that a non-stoichiometric Fe:Se ratio is critical for the occurrence of superconductivity [4] and initially it was supposed that this non-stoichiometry is a result of the formation of anion vacancies, which could stabilize the magnetic clusters [8]. However neutron scattering measurements suggest that anion sites are actually not vacant, but rather the excess Fe atoms occupy interstitial sites [9]. In order to evaluate which of these models is valid, we have studied the different structural models of non-stoichiometric $FeSe_x$ using density functional theory and Fe $L_{2,3}$ x-ray emission measurements.

2. Calculation and experimental details

Polycrystalline samples of $FeSe_x$ ($x = 0.85, 0.50$) were synthesized by a solid state reaction method using Fe and Se as starting materials. The raw materials were accurately weighed according to the selected ratio of $FeSe_x$, thoroughly ground, and pressed into pellets. The pellets were sealed in quartz tubes and were sintered at 700 °C for 24 h. The resulting product was reground thoroughly, pressed into pellets, and sealed in quartz

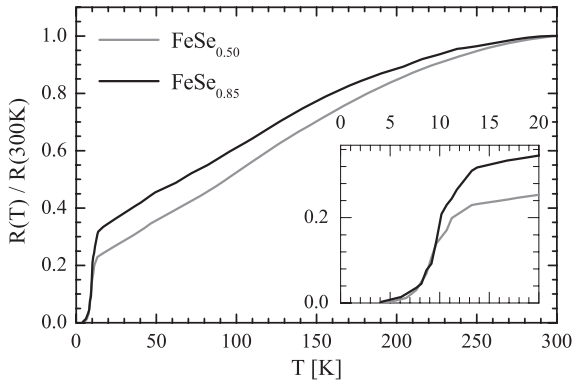

Figure 1. The temperature dependence of normalized electrical resistivity of $FeSe_x$ ($x = 0.85, 0.50$). The superconducting transition occurs at about 14 K.

tubes again. A second heat treatment was applied at 700 °C for 30 h.

The samples were characterized by x-ray diffractions (XRD) using Cu Kα radiation. The x-ray powder diffraction patterns show that all main peaks can be indexed by the tetragonal α-$FeSe_x$ ($P4/nmm$), with trace amounts of impurity hexagonal β-FeSe ($P6_3/mmc$), iron silicide, and Fe metal. The electrical transport was measured using the four-probe method with an alternating current (AC) resistance bridge system (Linear Research, Inc.; LR-700P). Figure 1 shows the temperature dependence of resistivity for the samples $FeSe_x$ ($x = 0.85, 0.50$). The superconducting transition is observed at about 14 K, and the behavior is the same as described in [4].

The soft resonant inelastic x-ray scattering measurements of $FeSe_x$ ($x = 0.85, 0.50$) were performed at the soft x-ray fluorescence endstation at Beamline 8.0.1 of the Advanced Light Source at Lawrence Berkeley National Laboratory [10]. The endstation uses a Rowland circle geometry x-ray spectrometer with spherical gratings and an area sensitive multichannel detector. The samples were mounted on carbon tape and measured at a 30° angle to the incident beam. We have measured resonant and non-resonant Fe $L_{2,3}$ (3d4s $\rightarrow$ 2p transition) x-ray emission spectra (XES). The instrumental resolving power ($E/\Delta E$) for XES was 1000. To determine the energies for resonant emission, x-ray absorption spectra (XAS) were obtained in both total electron yield (TEY) and total fluorescent yield (TFY) modes. The instrumental resolving power ($E/\Delta E$) for XAS was 5000. All spectra were normalized to the incident photon current using a highly transparent gold mesh in front of the sample to correct for intensity fluctuations in the incident photon beam.

Electronic structure calculations were performed with the full-potential linear augmented plane wave method as implemented in the WIEN2k code [11]. For the exchange–correlation potential we used the Perdew–Burke–Ernzerhof variant of the generalized gradient approximation [12]. The Brillouin zone integrations were performed with a $11 \times 11 \times 7$ k-point grid and $R_{\mathrm{MT}}^{\mathrm{min}}\, K_{\mathrm{max}} = 7$ (the product of the smallest of the atomic sphere radii R_{MT} and the plane wave cutoff parameter K_{max}) was used for the expansion of the basis

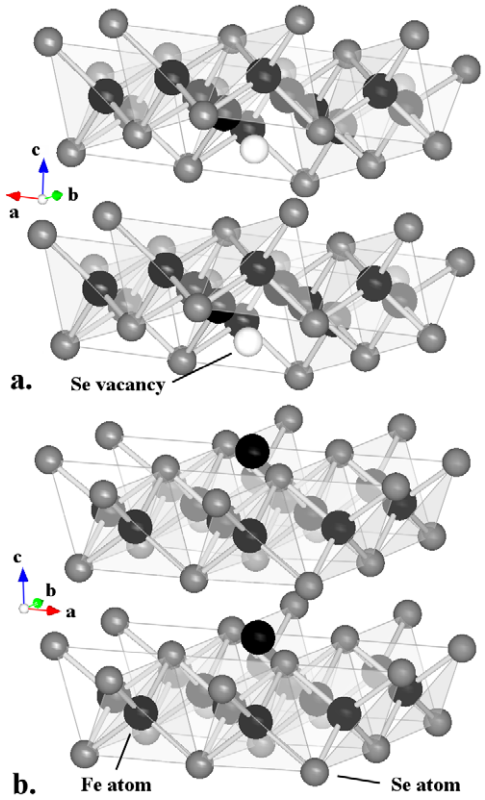

Figure 2. Crystal structure of structurally optimized FeSe with Se deficiencies ($FeSe_{1-1/8}$, section a), and interstitial Fe ($Fe_{1+1/8}Se$, section b).

(This figure is in colour only in the electronic version)

set. Atomic radii used were $R_{\mathrm{Fe}} = 2.19$ au and $R_{\mathrm{Se}} = 1.94$ au in both structures. The experimentally determined lattice parameters of tetragonal-phase FeSe ($a = 3.7676$ Å, $c = 5.4847$ Å) [4] were used. To calculate the electronic structure of FeSe with an excess of Fe or a deficit of Se, a $2a \times 2b$ supercell was constructed. The atomic positions in the $2a \times 2b$ supercell with one interstitial Fe atom or one Se vacancy site were optimized until the inter-atomic forces were smaller than 2 mRyd au^{-1}. The optimized structures belong to the space group $P4mm$. The coordinates of atoms and distances between Fe and Se atoms for the initial and optimized structures with interstitial Fe are displayed in table 1. The schematic crystal structures of $Fe_{1+1/8}Se$ and $FeSe_{1-1/8}$ are shown in figure 2. The interstitial Fe atoms were placed in the selenium plane and surrounded by a square planar arrangement of Se atoms. During the relaxation process interstitial Fe atoms were shifted upward into the interlayer region. The main effect of the Se vacancy on the structure was to shift the 4 Fe atoms surrounding the Se vacancy (the Fe_2 atoms in table 1) toward the vacant site, the remaining Fe atoms (the Fe_1 atoms in table 1) are affected little by the Se vacancy. The structural distortion in $FeSe_{1-1/8}$ agrees with that found in [8].

3. Results and discussion

The Fe $L_{2,3}$ XES and XAS measurements of $FeSe_{0.50}$ and $FeSe_{0.85}$ are shown in figure 3. The two main emission bands

Table 1. Structural parameters for the initial and optimized model of $Fe_{1+1/8}Se$ and $FeSe_{1-1/8}$. For the optimized model of $Fe_{1+1/8}Se$ the Fe–Se bond lengths are 2.32–2.34 Å and the Fe–Fe bond lengths are 2.51–2.68 Å. For the optimized model of $FeSe_{1-1/8}$ the Fe–Se bond lengths are 2.31–2.35 Å and the Fe–Fe bond lengths are 2.54–2.72 Å.

$Fe_{1+1/8}Se$	Fe_1	Fe_2	Fe_3	Se_1	Se_2	Se_3	Se_4
Wyckoff position	4e	4f	1a	4d	1a	2c	1b
Initial x	0.75	0.5	0.0	0.75	0.0	0.5	0.5
Initial y	0.0	0.75	0.0	0.75	0.0	0.0	0.5
Initial z	0.2434	0.2434	0.4868	0.4868	0.0	0.0	0.0
Optimal x	0.7535	0.5	0.0	0.7541	0.0	0.5	0.5
Optimal y	0.0	0.7506	0.0	0.7541	0.0	0.0	0.5
Optimal z	0.2365	0.2493	0.5447	0.4923	0.9758	0.9951	0.0035
$FeSe_{1-1/8}$	Fe_1	Fe_2	Fe_3	Se_1	Se_2	Se_3	Se_4
Wyckoff position	4f	4e	—	4d	2c	1b	—
Initial x	0.25	0.25	—	0.25	0.0	0.5	—
Initial y	0.5	0.0	—	0.25	0.5	0.5	—
Initial z	0.7657	0.7657	—	0.0	0.5314	0.5314	—
Optimal x	0.2490	0.2386	—	0.2456	0.0	0.5	—
Optimal y	0.5	0.0	—	0.2456	0.5	0.5	—
Optimal z	0.7700	7587	—	0.0107	0.5247	0.5260	—

in all the XES measurements correspond to the Fe L_3 ($3d4s \rightarrow 2p_{3/2}$ transitions) and Fe L_2 ($3d4s \rightarrow 2p_{1/2}$ transitions) normal emission lines separated by the spin–orbital splitting of Fe 2p states. The L_3 is sharp and similar to metallic iron [13] and in agreement with the related Fe 2p x-ray photo-emission spectra (XPS) of $FeSe_x$ [14], which shows a simple shape and absence of high-energy satellites typical for correlated FeO [15]. Both types of measurements (XES and XPS) suggest the Fe 3d electrons in $FeSe_x$ are somewhat itinerant in character. The resonant XES spectra (XES curves b, c, d in the bottom panels of figure 3) show no energy-loss features; this indicates that even resonant Fe $L_{2,3}$ XES probes mainly the partial occupied DOS in these materials. Note that the XES measurements of these materials were quite noisy, and especially in $FeSe_{0.50}$ the elastically scattered incident x-ray beam causes distortion; these should not be confused with energy-loss features. The XAS measurements in the top panel probe the unoccupied partial DOS (the conduction band), however the presence of a 2p Fe core-hole makes the local unoccupied 3d states more 'atomic-like' due to the greater effective nuclear charge, and is therefore not representative of the actual conduction band in the material. Further, the XAS TFY measurements show a large degree of self-absorption, which suppresses the main spectral features, and the XAS TEY measurements are highly surface sensitive. Since the samples were not cleaved *in situ*, there is almost certainly a fair amount of surface oxidation. For these reasons the XAS are presented here only to identify energies for resonant XES measurements.

The integral of the L_2 and L_3 bands in a non-resonant XES measurement are related to the population of the $2p_{1/2}$ and $2p_{3/2}$ states, respectively. For free atoms the ratio of the integrals of the L_2 and L_3 XES peaks (the $I(L_2)/I(L_3)$ ratio) should be equal to 1/2. In metals the radiationless $L_2L_3M_{4,5}$ Coster–Kronig (CK) transitions strongly reduce the $I(L_2)/I(L_3)$ ratio [16]. We have integrated the L_3 peak

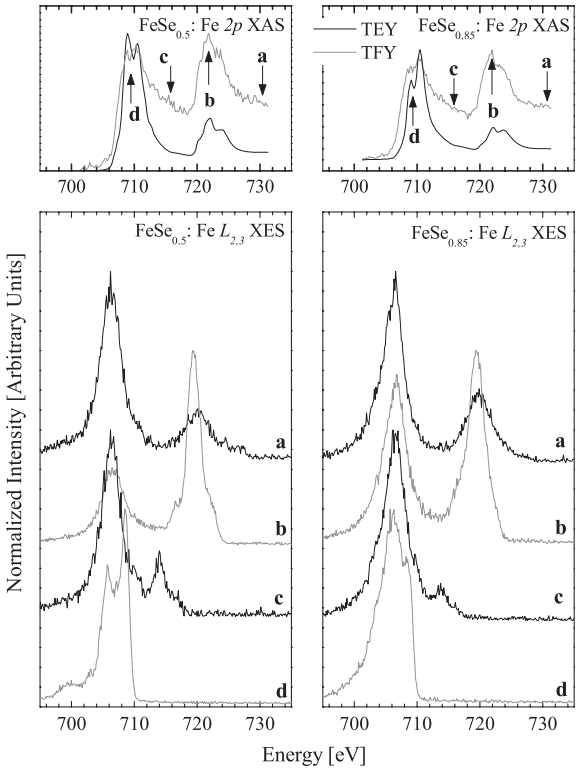

Figure 3. Summary of spectra for $FeSe_{0.50}$ (left side) and $FeSe_{0.85}$ (right side). The excitation energies for resonant Fe $L_{2,3}$ XES in the bottom panels are indicated by arrows in the XAS spectra in the top panels.

in the range 695–710 eV for FeO, 698–711 eV for both $FeSe_{0.50}$ and $FeSe_{0.85}$, and 698–708 eV for Fe metal, and the L_2 peak in the range 711–721 eV for FeO, 713–722 eV for both $FeSe_{0.50}$ and $FeSe_{0.85}$, and 714–722 eV for Fe metal. Figure 4 shows the $I(L_2)/I(L_3)$ ratio for $FeSe_{0.85}$ and $FeSe_{0.50}$ compared to that for Fe metal and FeO. The proximity of the $I(L_2)/I(L_3)$ ratio for $FeSe_{0.85}$ to that of FeO suggests that the 3d electrons are somewhat more localized than those in FeAs-type superconductors [17]. The $I(L_2)/I(L_3)$ ratio for $FeSe_{0.50}$ is between that of Fe metal and $FeSe_{0.85}$. This supports the idea that $FeSe_{0.50}$ is composed of $Fe_{1+x}Se$ with additional clusters of Fe metal [18]. The full width at half maximum (FWHM) of the L_3 band for $FeSe_{0.85}$ and $FeSe_{0.50}$ are consistent with that of Fe, the FWHM of the L_3 band in FeO is much larger. This illustrates that the bulk of the 3d Fe electrons are in a narrow band near the Fermi level, unlike in the electronic structure of FeO.

The calculated partial density of states for FeSe and the optimized structure $Fe_{1+1/8}Se$ and $FeSe_{1-1/8}$ are shown in figure 5. All materials have a band of 3d Fe electrons from 0 eV to about −2.5 eV, and a second band of hybridized 3d Fe and 4p Se electrons from about −3.2 eV to about −6 eV. The main difference between the DOS for each structure is the distribution of occupied states near the Fermi level. In FeSe the bulk of the 3d states are located in one prominent feature at ∼0.5 eV below the Fermi level. This feature is present in $FeSe_{1-1/8}$ as well, but is much less prominent. In $Fe_{1+1/8}Se$ the feature is just a minor peak, and the 3d

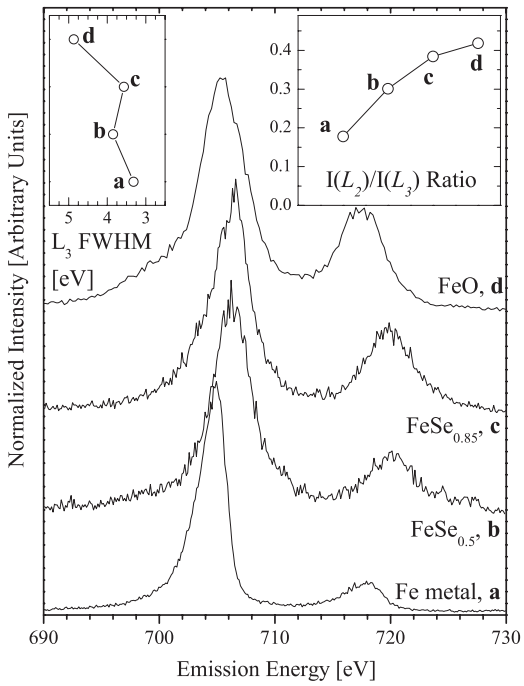

Figure 4. Comparison of the non-resonant $L_{2,3}$ XES spectra for metallic Fe, $FeSe_{0.50}$, $FeSe_{0.85}$, and FeO. The left inset shows the full width at half maximum (FWHM) of the Fe L_3 peak. The right inset shows the $I(L_2)/I(L_3)$ ratios for metallic Fe, $FeSe_{0.50}$, $FeSe_{0.85}$, and correlated FeO. The $I(L_2)/I(L_3)$ ratio was calculated from the ratios of the integral under the L_2 and L_3 peaks, respectively.

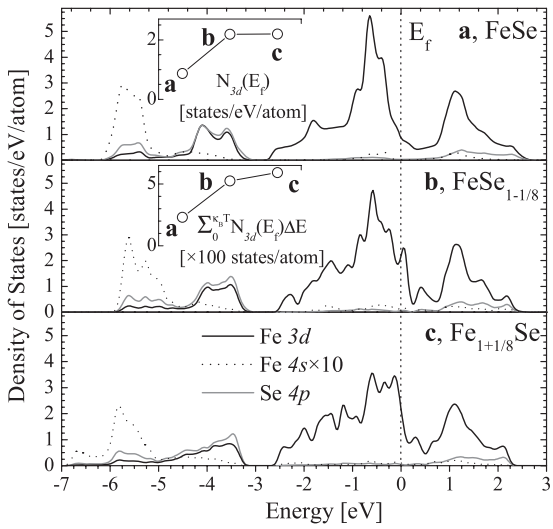

Figure 5. Calculated partial DOS for FeSe (panel a), $FeSe_{1-1/8}$ (panel b), and $Fe_{1+1/8}Se$ (panel c). The Fe 4s states are indicated by the dotted line, and increased by a factor of 10 for clarity. The top inset shows the density of states at the Fermi level, $N_{3d}(E_f)$ for each compound, and the middle inset shows the total number of occupied states within $\kappa_B T$ (for $T = 300$ K) of the Fermi level. The temperature $T = 300$ K is somewhat arbitrary (300 K was chosen because the x-ray measurements were taken at room temperature), but the trend shown in the inset is consistent for temperatures less than $T = 300$ K as well.

states are more evenly distributed. Both $Fe_{1+1/8}Se$ and $FeSe_{1-1/8}$ have the same number of 3d states at the Fermi level (2.19 states/eV/atom) while FeSe has far fewer (only 0.87 states/eV/atom). Despite equal contributions at the Fermi level, $Fe_{1+1/8}Se$ has more occupied states close to the Fermi level. $Fe_{1+1/8}Se$ has 13% more states within the thermal energy at room temperature ($\kappa_B T$) than $FeSe_{1-1/8}$ (0.0592 states/atom compared to 0.0524 states/atom for $FeSe_{1-1/8}$). Since a large number of Fermi level 3d states are present in FeAs-type materials [19], this suggests that $Fe_{1+1/8}Se$ is the correct structural model for superconducting $FeSe_x$-type materials.

Due to the rather poor signal-to-noise ratio in the XES measurements, a curve-fitting approach was used to compare the x-ray spectra to the calculated partial DOS. Only the L_3 band of the non-resonant XES spectra were fit, since the L_2 band is the same basic shape as the L_3 band but with poorer statistics and the resonant XES spectra were distorted by the elastically scattered incident x-ray beam. To ensure that the results were free of bias, between one and six pseudo-Voigt components were fit to the XES data by minimizing the least-squares residuals between the fit and the data. The components were of the form shown in equation (1). For a given number of pseudo-Voigt components a number of different fits were attempted, each starting from a different selection of initial guesses for the center points μ_i. The results were essentially equivalent for 'reasonable' guesses of μ_i (i.e. components centered within the L_3 band). The quality of the fit was measured using the parameter $F'' = \sqrt{\sum_x (f_{data}(x) - f_{fit}(x))^2}$, and the 'simplest best fit' was chosen as the fit with the fewest number of components that produced an F'' parameter consistent with more complicated fits.

$$f_V = A(\eta f_G + (1-\eta) f_L)$$
$$f_G = \frac{1}{\sqrt{2\pi}\sigma} \exp\left(-\frac{(x-\mu)^2}{2\sigma^2}\right) \qquad (1)$$
$$f_L = \frac{1}{\pi}\left(\frac{\frac{\Gamma}{2}}{(x-\mu)^2 + \left(\frac{\Gamma}{2}\right)^2}\right).$$

For both materials, the 'simplest best fit' had only two pseudo-Voigt components, as shown in figure 6. We should point out that the generally poor signal-to-noise ratio in $FeSe_{0.50}$ make accurate curve-fitting difficult; indeed the 'best' fit for $FeSe_{0.50}$ appears to have five pseudo-Voigt components (see the inset in the lower panel of figure 6). However the three extra components in this fit are extremely sharp, low amplitude curves that essentially fit the noise in the spectrum. Therefore only the two component fit is reported in detail here. For $FeSe_{0.85}$ there is a clear statistical difference between a single component and a two component fit; adding more components does not improve the quality of the fit very much (see the inset in the upper panel of figure 6). The mixing factor η was held constant for all pseudo-Voigts in a fit, and the Gaussian width σ was set to the instrumental broadening ($\mu_i \times \Delta E/E$). The parameters of the best fits for each material are summarized in table 2.

The calculated partial occupied DOS for $FeSe_{1-1/8}$ and $Fe_{1+1/8}Se$ has three basic features within the energy range of the Fe 3d L_3 band: the feature near the Fermi level (region

Table 2. Fit results for the two pseudo-Voigt peaks for fitting the Fe L_3 XES of $FeSe_{0.50}$, and the both the two and three pseudo-Voigt peaks fit results for $FeSe_{0.85}$. Note there is only one mixing factor η for all components in the same spectrum.

	η_i	A_i	μ_i (eV)	Γ_i (eV)
$FeSe^{(1)}_{0.50}$	0.07	2.53	705.6	3.80
$FeSe^{(2)}_{0.50}$		2.56	704.3	4.12
$FeSe^{(1)}_{0.85}$	0.04	1.57	705.5	2.08
$FeSe^{(2)}_{0.85}$		4.15	704.2	5.60
$FeSe^{(i)}_{0.85}$	0.05	1.75	705.5	2.22
$FeSe^{(ii)}_{0.85}$		3.78	704.2	5.63
$FeSe^{(ii)}_{0.85}$		0.06	701.8	0.79

a in figure 6), the broad group of states just below the main feature (region b in figure 6), and the separate group of states hybridized with Se 4p and Fe 4s states (region c in figure 6). Because of the spectral broadening that occurs in core-level spectroscopy, we expect the main feature (region a) to be the most prominent part of the XES band due to the large DOS and proximity to the Fermi level (where lifetime broadening effects are the smallest [20]). The remaining features we expect to be smeared into one (for both b and c regions together) or at most two (for b and c regions separately) additional XES features. Indeed, the curve-fitted components of $FeSe_{0.85}$ (see table 2) are in good agreement with the calculated partial occupied DOS for both $FeSe_{1-1/8}$ and $Fe_{1+1/8}Se$, as shown in the top and middle panels of figure 6. The three component curve-fit for $FeSe_{0.85}$ lines up well with the three DOS regions discussed above, shown in the middle panel of figure 6 but note that the third component is located near 702 eV and is very small. While we suspect that this third component indeed represents a third XES feature (and not just spectral noise), statistically we are not justified in considering the three component fit as more accurate than the two component fit.

The two component curve-fits for both $FeSe_{0.85}$ and $FeSe_{0.50}$ are a reasonable match to the calculated DOS. Since the Fe $L_{2,3}$ probes the partial DOS, we expect the integral of each component curve to be proportional to the number of states represented by that feature. For $Fe_{1+1/8}Se$ there are roughly 3.5 states/atom in regions b and c, and 2.4 states/atom in region a (there are 6 Fe 3d states/atom in total, about 0.1 states/atom are distributed in a broad band below region c). For $FeSe_{1-1/8}$ there are roughly 3.1 states/atom in regions b and c, and 2.8 states/atom in region a (again, about 0.1 states/atom are deeper in the valence band). The integrals of the two component curves of $FeSe_{0.85}$ are 1.57 for the curve near the Fermi level, and 4.15 for the curve deeper in the valence band (see table 2, note that the amplitude of the curve is the same as the integral). The ratio between the integrals of these two curves ($\sim$0.38) is closer to the ratio in the total states between region a and regions b, c for $Fe_{1+1/8}Se$ ($\sim$0.69) than the same ratio in $FeSe_{1-1/8}$ ($\sim$0.90). This further supports our conclusion that $FeSe_x$ is made of FeSe with interstitial Fe rather than FeSe with Se vacancies.

To summarize, we have studied $FeSe_x$ ($x = 0.85$, 0.50) with soft x-ray spectroscopy and density functional theory

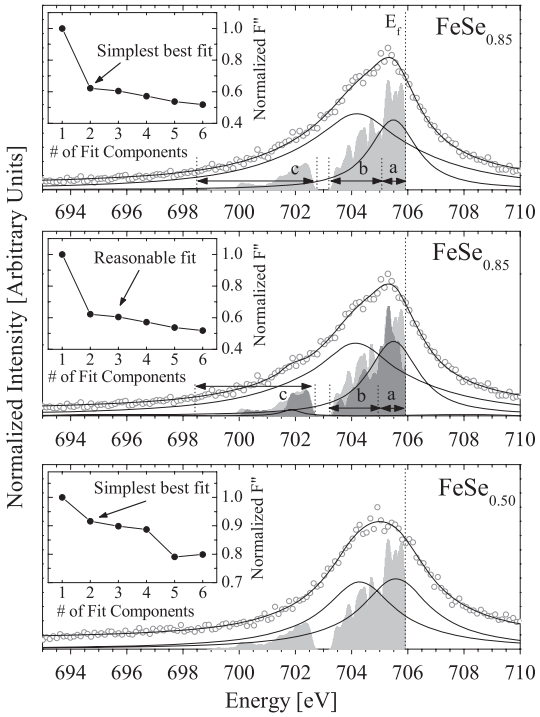

Figure 6. Comparison of calculated DOS and measured non-resonant L_3 XES. The top panel shows the L_3 peak of the Fe $L_{2,3}$ spectrum, the Fe 3d DOS of $Fe_{1+1/8}Se$, best-fit curve, and the 2 pseudo-Voigt components contributing to the best-fit curve for $FeSe_{0.85}$. The center panel shows the L_3 peak of the Fe $L_{2,3}$ spectrum, the Fe 3d DOS of both $Fe_{1+1/8}Se$ (light gray) and $FeSe_{1-1/8}$ (dark gray), best-fit curve, and the 3 pseudo-Voigt components contributing to the next simplest curve-fit for $FeSe_{0.85}$. The bottom panel shows the L_3 peak of the Fe $L_{2,3}$ spectrum, the Fe 3d DOS of $Fe_{1+1/8}Se$, best-fit curve, and the 2 pseudo-Voigt components contributing to the best-fit curve for $FeSe_{0.50}$. The insets show the normalized fit parameter F'' for fits with different numbers of pseudo-Voigt components for each material. Note that the maximum F'' has been scaled to 1.0 in each case. The estimated Fermi level is indicated in each plot.

calculations. The $Fe_{1+1/8}Se$ structural model of tetragonal FeSe with excess interstitial Fe matches the experimental results better than the $FeSe_{1-1/8}$ model of tetragonal FeSe with Se vacancies. There is also evidence that $FeSe_x$ ($x \lesssim 0.89$) is composed of $Fe_{1+1/8}Se$ with clusters of Fe metal. The interstitial Fe increases the Fe 3d occupied DOS near the Fermi level, suggesting that the interstitial Fe is responsible for the superconductivity in $FeSe_x$.

Acknowledgments

We acknowledge support of the Research Council of the President of the Russian Federation (Grants NSH-1929.2008.2 and NSH-1941.2008.2), the Russian Science Foundation for Basic Research (Project 08-02-00148), the Natural Sciences and Engineering Research Council of Canada (NSERC), and the Canada Research Chair program.

References

[1] Kamihara Y, Hiramatsu H, Hirano M, Kawamura R, Yanagi H, Kamiya T and Hosono H 2006 *J. Am. Chem. Soc.* **128** 10012

[2] Rotter M, Tegel M and Johrendt D 2008 *Phys. Rev. Lett.* **101** 107006
[3] Pitcher M J, Parker D R, Adamson P, Herkelrath S J C, Boothroyd A T, Ibberson R M, Brunelli M and Clarke S J 2008 *Chem. Commun.* **45** 5918
[4] Hsu F-C *et al* 2008 *Proc. Natl Acad. Sci.* **105** 14262
[5] Mizuguchi Y, Tomoika F, Tsuda S, Yamaguchi T and Takano Y 2008 *Appl. Phys. Lett.* **93** 152505
[6] Subedi A, Zhang L, Singh D and Du M 2008 *Phys. Rev.* B **78** 134514
[7] Qui Y *et al* 2009 *Phys. Rev. Lett.* **103** 067008
[8] Lee K-W, Pardo V and Pickett W E 2008 *Phys. Rev.* B **78** 174502
[9] Bao W *et al* 2009 *Phys. Rev. Lett.* **102** 247001
[10] Jia J J *et al* 1995 *Rev. Sci. Instrum.* **66** 1394
[11] Blaha P, Schwarz K, Madsen G K H, Kvasnicka D and Luitz J 2001 *WIEN2k, An Augmented Plane* Wave + Local *Orbitals Program for Calculating Crystal Properties* Karlheinz Schwarz, Techn. Universität Wien, Austria ISBN 3-9501031-1-2
[12] Perdew J P, Burke K and Ernzerhof M 1996 *Phys. Rev. Lett.* **77** 3865
[13] Gao X, Qi D, Tan S C, Wee A T S, Yu X and Moser H O 2006 *J. Electron. Spectrosc. Relat. Phenom.* **151** 199
[14] Yamasaki A *et al* 2009 arXiv:0902.3314 [cond-mat]
[15] Galakhov V R, Poteryaev A I, Kurmaev E Z, Anisimov V I, Bartkowski St, Neumann M, Lu Z W, Klein B M and Zhao T-R 1997 *Phys. Rev.* B **56** 4584
[16] Kurmaev E Z, Ankudino A L, Rehr J J, Finkelstein L D, Karimov P F and Moewes A 2005 *Electron Spectrosc. Relat. Phenom.* **148** 1
[17] Kurmaev E Z, McLeod J A, Buling A, Skorikov N A, Moewes A, Neumann M, Korotin M A, Izyumov Yu A, Ni N and Canfield P C 2009 *Phys. Rev.* B **80** 054508
[18] Okamoto H 1991 *J. Phase Equilib.* **12** 383
[19] Singh D J 2008 *Phys. Rev.* B **78** 094511
[20] Goodings D A and Harris R 1969 *J. Phys. C: Solid State Phys.* **2** 1808